
This manuscript is a preprint that has been submitted to a peer-reviewed journal. The manuscript is yet to be reviewed, thus, subsequent versions of this manuscript may have different content. If accepted, the final version of this manuscript will be available via the 'Peer-reviewed Publication DOI' link. Please feel free to contact Dr Chris Yeomans (c.m.yeomans@exeter.ac.uk) to comment on the manuscript. We welcome feedback.

Highlights

Application of the tilt derivative transform to bathymetric data for structural lineament mapping

Christopher M. Yeomans, Matthew Head, Jordan J. Lindsay

- High-resolution bathymetric data are used to analyse submerged outcrops for structural lineaments
- Steps in bathymetry cause problems when enhancing lineaments using common feature extraction methods
- The tilt derivative transform successfully enhances lineaments prior to lineament extraction

Application of the tilt derivative transform to bathymetric data for structural lineament mapping

Christopher M. Yeomans^{a,*}, Matthew Head^a and Jordan J. Lindsay^a

^a*Camborne School of Mines, College of Engineering, Mathematics and Physical Sciences, University of Exeter, Penryn Campus, Penryn, Cornwall, TR10 9FE, UK*

ARTICLE INFO


Keywords:

Tilt derivative transform
Bathymetry
Lineament detection
Object-based Image Analysis
Southwest England

ABSTRACT

High-resolution bathymetry surveys provide an opportunity to analyse local geological structure where onshore areas afford limited exposure. Semi-automated lineament detection methods are necessary for areas of large coverage where a manual analysis would be subjective and time-consuming. However, semi-automated approaches are dependent on effective feature extraction methods to identify genuine lineaments. This study offers solutions to common problems that can impede processing methods where sharp steps in the seafloor (e.g. palaeocoastlines) are present. Directional gradient, Sobel and Laplacian filters are explored as well as the hillshade and tilt derivative transform for feature extraction prior to applying an object-based image analysis lineament detection approach. The filtered datasets generally perform poorly with a marked improvement when using the hillshade transform. However, we find the azimuth-invariant tilt derivative, which incorporates a convolved vertical derivative, to be the most successful, identifying lineaments in a range of orientations and across a sharp step in the seafloor.

*Corresponding author

 c.m.yeomans@exeter.ac.uk (C.M. Yeomans)

ORCID(s): 0000-0002-0364-451X (C.M. Yeomans); 0000-0003-0103-8329 (.M. Head); 0000-0003-2190-4116 (J.J. Lindsay)

1. Introduction

The bathymetry of the seafloor is complementary to the topography of the land and can describe various morphological features in the marine environment such as sedimentary bedforms or submerged outcrop (Hell et al., 2012). Bathymetric models produce a continuous surface of the seabed and provide an excellent means for viewing the structural complexity of exposed bedrock (Collier et al., 2006; Nixon et al., 2012). High-resolution data are particularly effective at defining areas of submerged outcrop and capture the detail of geological structure including bedding of strata and cross-cutting faults where these features dip $>10^\circ$ (Collier et al., 2006). Bathymetric data has also been shown to enhance the interpretation of seismic reflection data to better understand the geometry of structures and stratigraphy (Collier et al., 2006; Sanderson et al., 2017; Westhead et al., 2018).

Bathymetric data has been employed in a variety of studies to map geological structure and to enhance the interpretation of seismic reflection data (e.g. Collier et al., 2006; Nixon et al., 2012; Sanderson et al., 2017; Westhead et al., 2018). In some cases, bathymetric models can be derived from 3D seismic data, but generally multi-beam phase-difference methods are preferred (Power and Clarke, 2019). Remote mapping of seafloor lineaments complements land-based studies to help define the structural evolution of an area. Where submerged outcrop can be identified, high-resolution bathymetric data can provide an excellent input dataset for lineament detection. The data capture the detail of geological structure including bedding of strata and cross-cutting faults where these features dip $>10^\circ$ (Collier et al., 2006). The extensive coverage available for these studies, often at high-resolution, can be cumbersome for manual methods. The ability to semi-automate lineament extraction and loop through a range of azimuths has meant that more objective lineament maps can be created compared to manual methods (e.g. Rahnama and Gloaguen, 2014; Middleton et al., 2015; Šilhavý et al., 2016; Yeomans et al., 2019). Therefore, a semi-automated lineament detection method can be desirable and increase the objectivity of the analysis. However, semi-automated methods require prior feature extraction to enhance data and target desirable structures. This is key for mapping offshore lineaments and poor feature extraction can be detrimental to the analysis.

This study investigates the effectiveness of different operators as a means for feature extraction, including direc-

25 tional gradient and Sobel filters, azimuth-invariant Laplacian filters as well as transforms such as hillshading and the
26 tilt derivative (TDR). It is worth noting that the use of directional filtering has become less popular over time due to
27 the availability of more rigorous algorithms (Airo, 2013). However, many studies still implement the use of directional
28 filters as a first pass for lineament mapping (Mallast et al., 2011; Sedrette and Rebaï, 2016). The study uses bathymetric
29 data from SW England over a classic area of offshore NW Devon, illustrated in Figure 1 and utilises a state-of-the-art
30 Object-based Image Analysis (OBIA) lineament detection method designed by Yeomans et al. (2019). A small subset
31 of the study area over the platform edge is highlighted; full analyses are included in the Supplementary Information.

32 Understanding how different filters and transforms affect the final lineament population is important for selecting
33 the most appropriate feature extraction tool when applying semi-automated methods. The different visualisations tested
34 here test the importance of not only weighting azimuth equally but also examines how vertical changes in bathymetry
35 can affect the results. Furthermore, we examine means of semi-automatically identifying areas of sediment cover that
36 may lead to false positive lineaments and the potential effect of those spurious results if not removed. The study forms
37 a precursor prior to lineament detection and structural analysis of offshore areas at a regional scale.

38 **1.1. Geological setting**

39 The geology of the study area comprises Culm Basin rocks which were deformed during Variscan orogenesis
40 creating gently plunging chevron folds and predominantly NNW-directed thrusts (Rattee and Sanderson, 1984; Holder
41 and Leveridge, 1986; Lloyd and Chinnery, 2002; Leveridge and Hartley, 2006). During this time, strike-slip transfer
42 faults were formed in a NW to NNW orientation (Leveridge et al., 2002). Intraplate tectonics brought about subsequent
43 phases of extension during the Permo-Triassic (Shail and Alexander, 1997). This was followed by the onset of Atlantic
44 opening in the latest Jurassic-Cretaceous before Alpine collision caused minor inversion and substantial Cenozoic
45 strike-slip movement (Holloway and Chadwick, 1986; Cheadle et al., 1987; Chapman, 1989; Hillis et al., 2008). These
46 NW-SE structures, and subordinate NNE-SSW structures, have been reactivated multiple times during this period
47 (Shail and Alexander, 1997; Ault et al., 2016), and have previously been investigated by Nixon et al. (2012) and
48 Nyberg et al. (2018). They form the target for semi-automated lineament detection in this study and are of particular
49 importance for understanding the post-Variscan structural evolution of the region.

50 **2. Data and methods**

51 Manual lineament extraction studies can be effective at identifying structural features and creating maps of fault
52 systems (e.g. Nixon et al., 2012). These studies often produce maps with long lineament traces that appear robust but
53 can be subjective and dependent on the visualisation method (Scheiber et al., 2015). Biases can exist in various aspects
54 of a manual analysis including lineament length and the scale/detail of fractures mapped, although user experience
55 appears to be less important (Andrews et al., 2019). Semi-automated methods can mitigate these biases but the data
56 often still require enhancement via feature extraction methods; thus requiring careful consideration. Directional filters
57 such as gradient and Sobel kernels are effective at finding lineaments where the orientation is known; the same holds for
58 the hillshade transform. Where this is not the case, the method must be azimuth-invariant and weight all orientations
59 equally (e.g. Laplacian filters). Changes in the vertical plane of the source data can also influence the outputs, which
60 is why the tilt derivative (TDR) transform is investigated in this study and compared to the aforementioned filters and
61 hillshade transform.

62 **2.1. Bathymetric data**

63 The area of interest selected for this study is in the region offshore of Hartland Point, Devon (Figure 1b). Bathy-
64 metric data were downloaded at 2 m pixel resolution from the United Kingdom Hydrographic Office (UKHO) via
65 the Admiralty Data Portal. These data have been collected as multibeam bathymetry through several surveys from
66 2007-2008; full details can be found in Supplementary Information. The site covers an area of submerged outcrop
67 with a distinct platform area curtailed to the north of the study by an apparent palaeocoastline. This on-platform area
68 extends some 2800 m west of the present coastline with a gentle gradient into deeper off-platform areas whereas to the
69 north the on-platform area extends approximately 2300 m where a sharp drop >10 metres in the platform occurs over
70 a palaeocoastline. Although sand cover becomes problematic in the westernmost part of the area, it is largely limited
71 to the nearshore coves with small pockets found along the palaeocoast. The area was featured as part of a manual
72 lineament analysis by Nixon et al. (2012) who determined a series of NW-SE and NNE-SSW trending fault sets that
73 exhibit dextral and sinistral offsets, respectively. The area is also used as a case study site to showcase the NetworkGT
74 plug-in for QGIS software, which consists of a suite of tools for geometric and topological analysis of two-dimensional

75 fracture networks (Nyberg et al., 2018). Both Nixon et al. (2012) and Nyberg et al. (2018) have demonstrated that the
76 area provides an excellent site for studying fault networks and this study will aim to extend this into deeper water.

77 **2.2. Filters and transforms**

78 Geospatial data, even after all processing steps have been completed, almost always require some further ma-
79 nipulation to enhance certain features prior to further analysis; for image or raster data, this often involves a filter or
80 transform. There are a broad range of enhancements that can be tailored to the task and, when used with an appropriate
81 semi-automated algorithm, a high degree of accuracy can be achieved (Sukumar et al., 2014). However, determining
82 a suitable image enhancement can be difficult and potentially subjective especially depending on the target structure
83 and the signal-to-noise ratio (Smith and Clark, 2005; Rahnama and Gloaguen, 2014).

84 Band pass filters, such as the gradient and Sobel operators, are effective at selecting a particular range (based on
85 directionality). Low-pass and high-pass filters are useful for mitigating noise and enhancing the sharpness of features,
86 respectively (Rahnama and Gloaguen, 2014). Transforms do not preferentially select data but convert the whole dataset
87 to derive a new variable.

88 In this study, the directional gradient, Sobel and Laplacian filters as well as the hillshade and TDR transforms
89 have been selected to demonstrate various feature extraction methods. These operators have been selected as they
90 are commonly applied in lineament detection studies, be it manual or semi-automated, to enhance features prior to
91 detection on a variety of datasets (Smithurst, 1990; Morris, 1991; Maini and Aggarwal, 2009; Airo and Wennerström,
92 2010; Mallast et al., 2011; Grebby et al., 2012; Hashim et al., 2013; Rahnama and Gloaguen, 2014; Sukumar et al.,
93 2014; Middleton et al., 2015; Mwaniki et al., 2015; Scheiber et al., 2015; Sedrette and Rebaï, 2016; Šilhavý et al.,
94 2016; Thiele et al., 2017; Yeomans et al., 2019; Xu et al., 2020). It is worth noting that other methods are available
95 such as the Prewitt filter, Canny filter (Canny, 1986), Principal Component Analysis (e.g. Grebby et al., 2012), Hough
96 transforms (e.g. Han et al., 2018) and geomorphological features (Kokinou and Panagiotakis, 2018) among others,
97 which fall out of scope of this study.

98 **2.2.1. Directional filters**

99 Directional filtering of spatial data is a well-established tool used to highlight features for lineament detection and
 100 structural mapping. The filter uses a weighted kernel to accentuate particular-oriented features, where features are
 101 perpendicular to the overall gradient of weights within the kernel. The use of directional filters was detailed by Moore
 102 and Waltz (1983) who provided a five-step framework for lineament enhancement that included smoothing, directional
 103 filtering, smoothing directional components, lineament extraction and scaling. For a 3 x 3 matrix, the process takes
 104 the focal pixel, A_0 , and surrounding pixels ($B, C...I$) from the input data λ in Equation 1:

$$\lambda_3 = \begin{bmatrix} B & C & D \\ E & A_0 & F \\ G & H & I \end{bmatrix} \quad (1)$$

105 Or, for a 5 x 5 matrix, Equation 2:

$$\lambda_5 = \begin{bmatrix} B & C & D & E & F \\ G & H & I & J & K \\ L & M & A_0 & N & O \\ P & Q & R & S & T \\ U & V & W & X & Y \end{bmatrix} \quad (2)$$

106 The values in λ are convolved by a directional kernel in Equation 3 containing, in this case, a northwest gradient:

$$G_{NW} = \begin{bmatrix} -2 & -1 & 0 \\ -1 & 0 & 1 \\ 0 & 1 & 2 \end{bmatrix} * \lambda_3 \quad (3)$$

107 or a northeast gradient using Equation 4:

$$G_{NE} = \begin{bmatrix} 0 & -1 & -2 \\ 1 & 0 & -1 \\ 2 & 1 & 0 \end{bmatrix} * \lambda_3 \quad (4)$$

108 The results of these orthogonal filters can be combined as a magnitude using Equation 5:

$$|G| = \sqrt{G_{NW}^2 + G_{NE}^2} \quad (5)$$

109 The weights used here have been chosen to emphasise the main directions of known faults in the study area.
 110 However, directional filtering can vary considerably depending on the task in hand, but generally take the form of a 3
 111 x 3 kernel where the direction of positive-to-negative weighting provides the orientation of the kernel.

112 2.2.2. Sobel filter

113 The Sobel filter is a commonly used edge detector technique and allows the calculation of the X and Y derivatives
 114 with a level of smoothing imparted via the kernel (Sobel and Feldman, 1973; Favalli and Fornaciai, 2017). It is another
 115 directional gradient-based method where the X and Y derivatives for the Sobel filter are calculated using Equation 6
 116 and Equation 7, respectively.

$$G_H = \begin{bmatrix} 1 & 0 & -1 \\ 2 & 0 & -2 \\ 1 & 0 & -1 \end{bmatrix} * \lambda_3 \quad (6)$$

$$G_V = \begin{bmatrix} 1 & 2 & 1 \\ 0 & 0 & 0 \\ -1 & -2 & -1 \end{bmatrix} * \lambda_3 \quad (7)$$

117 These two first-order derivatives can then be combined into a gradient magnitude image using Equation 8:

$$|G| = \sqrt{G_H^2 + G_V^2} \quad (8)$$

118 The Sobel filter is most sensitive to lineaments in the X and Y directions and diagonal components can be sup-
 119 pressed (Sobel and Feldman, 1973). The Sobel filter is essentially a modification of the Prewitt filter which does not
 120 account for smoothing. The introduction of a -2 weight to the filter (compared to a -1 for the Prewitt filter) adds a more
 121 'circular' operation to the kernel that is advantageous over the Prewitt filter (Davies, 1986).

122 2.2.3. Laplacian filter

123 The Laplacian filter is a second-order derivative, non-directional filtering tool that has been widely applied for
 124 detecting structural lineaments from remotely sensed data (e.g. Grebby et al., 2012; Rahnama and Gloaguen, 2014;
 125 Al-Azemi and Divi, 2017). The Laplacian can be derived using Equation 9, which can be approximated by convolving
 126 the matrices described in Equation 10 and Equation 11 for a 3 x 3 kernel and 5 x 5 kernel, respectively.

$$L_{(x,y)} = \nabla^2 f_{(x,y)} = \frac{\delta^2 f(x,y)}{\delta x^2} + \frac{\delta^2 f(x,y)}{\delta y^2} \quad (9)$$

$$L_3 = \begin{bmatrix} 0 & -1 & 0 \\ -1 & 4 & -1 \\ 0 & -1 & 0 \end{bmatrix} * \lambda_3 \quad (10)$$

$$L_5 = \begin{bmatrix} 0 & 0 & -1 & 0 & 0 \\ 0 & -1 & -2 & -1 & 0 \\ -1 & -2 & 17 & -2 & -1 \\ 0 & -1 & -2 & -1 & 0 \\ 0 & 0 & -1 & 0 & 0 \end{bmatrix} * \lambda_5 \quad (11)$$

127 The Laplacian filter is useful as it returns a smoother image where edges are located at the zero-contour (Marr and
 128 Hildreth, 1980). Being a second-order derivative, the Laplacian filter is more sensitive to noise in the data and may
 129 also be prone to edge-effects in the data (Maini and Aggarwal, 2009). Other derivations of the filter can mitigate this by
 130 combining Gaussian smoothing to enhance edge detection (e.g. Maini and Aggarwal, 2009; Rahnama and Gloaguen,
 131 2014).

132 2.2.4. Hillshade transform

133 A shaded relief, or hillshade transformation, is a common tool for visualising topographic data and a useful first
 134 step for lineament mapping (Höfle and Rutzinger, 2011; Scheiber et al., 2015; Favalli and Fornaciai, 2017). It involves
 135 transforming a 2D image to highlight features in a particular direction based on a theoretical sun position; assuming
 136 a Lambertian surface and single light source at an infinite distance (Favalli and Fornaciai, 2017). The sun position
 137 is defined by an *azimuth* (A_s) and *zenith* (Z_s) and is combined with a *slope* (S_e) and *aspect* (A_e) derived from the
 138 elevation model to calculate the hillshade (H) image (Equation 12) where all all angles are converted to radians.

$$H = 255 * ((\cos(Z_s) * \cos(S_e)) + (\sin(Z_s) * \sin(S_e) * \cos(A_s - A_e))) \quad (12)$$

139 Shadows are imparted on the image based on the azimuth and zenith of the light source where a zenith of zero
 140 would place the sun on the horizontal plane of reference. The single light source results in azimuth biasing and can
 141 change the apparent position of breaks in slope as well as the apparent convexity or concavity of a feature (Smith and
 142 Clark, 2005; Favalli and Fornaciai, 2017). This can be mitigated by using multiple hillshade images where at least two
 143 images are generated parallel, and orthogonal, to the principal lineament orientation to capture the main trends (Smith

144 and Clark, 2005). This approach is similar to the methods of directional filters but is not as limited in orientation and
 145 the *zenith* imparts a level of sensitivity. However, lower zenith angles can lead to a loss of detail in shaded areas
 146 adjacent to prominent topography.

147 2.2.5. Tilt derivative transform

148 The tilt derivative (TDR) transform was first described by Miller and Singh (1994) whereby a tilt angle is deter-
 149 mined by the arctangent of the vertical and total horizontal derivative of the data (T) (Equation 13). The transform
 150 was developed for use with potential field data, primarily magnetic data, but has since been applied to other datasets
 151 such as LiDAR data (Middleton et al., 2015) and the Total Count of radiometric data (Yeomans et al., 2019) where the
 152 vertical derivative is calculated through convolution.

$$TDR = \tan^{-1} \left(\frac{\frac{\partial T}{\partial z}}{\sqrt{\left(\frac{\partial T}{\partial x}\right)^2 + \left(\frac{\partial T}{\partial y}\right)^2}} \right) \quad (13)$$

153 The TDR transform is a useful tool for preserving low amplitude signals which may be attenuated over the dynamic
 154 range in the presence of a larger amplitude signal (Miller and Singh, 1994; Verduzco et al., 2004; Fairhead et al.,
 155 2004). Values are restricted to $\pm\pi/2$ by the arctangent function, regardless of the derivative magnitudes, preserving
 156 low amplitude signals and reducing the effect of noise. Additionally, this feature assists the interpretation where the
 157 continuity of a body may vary due to lateral changes in signal (Verduzco et al., 2004). Furthermore, the zero-contour
 158 passes over or near the edge of bodies (Miller and Singh, 1994). These features make the TDR transform an effective
 159 tool for mapping edges or mapping minima/maxima.

160 2.3. Lineament detection

161 Lineament detection techniques have commonly taken a pixel-based approach to feature identification. The results
 162 have shown broad improvement over several decades but are still fallible in noisy data and in areas where lineaments
 163 appear discontinuous. Object-Based Image Analysis (OBIA) workflows allow the generation of spatially correlated
 164 groups of pixels or “image objects” to identify lineaments. The advantage of an OBIA approach is that objects have

165 internal and relative statistics as well as a geospatial topology that can hone the classification (Lang, 2008). The use
166 of these attributes can result in a more subjective assessment (Blaschke et al., 2004) but the analysis is more robust
167 to noise compared to pixel-based methods (Van Den Eeckhaut et al., 2005, 2012). Image objects have proven an
168 effective means for lineament detection and used on a variety of data types including spaceborne InSAR and Landsat
169 data (Mavrantza and Argialas, 2006; Marpu et al., 2008), as well as airborne LiDAR, magnetic and radiometric data
170 (Rutzinger et al., 2006; Middleton et al., 2015; Yeomans et al., 2019).

171 Herein, an OBIA workflow is used to capture lineaments in the bathymetry. Prior to the analysis, outliers were
172 removed and the ranges for each filter and the hillside transform were linearly transformed to optimise performance
173 within the algorithm; see Supplementary Information. The data are taken as a single input layer using the bottom-
174 up OBIA method described by Yeomans et al. (2019). The method efficiently performs lineament extraction from
175 large raster datasets whilst creating slightly shorter lineament segments compared to top-down OBIA methods (e.g.
176 Middleton et al., 2015; Yeomans et al., 2019). For this study, line extraction was completed in two phases and optimised
177 for each data input. The first phase searched for NW-SE lineaments in the range 120° to 175° using a line width of 2
178 pixels, the second phase targeted NNE-SSW lineaments in the range 005° to 060° with a line width of 1 pixel. The
179 resultant image objects were then merged and processed as per the approach outlined in Yeomans et al. (2019). Note
180 that lineaments between 060° and 120° were purposefully not included in the detection ranges for the two phases as
181 these equate to bedding surfaces that varied due to tight fold axes.

182 **3. Results and discussion**

183 In this section, we present visualisations using each of the filters and transforms introduced above and the subse-
184 quent derived lineaments. The semi-automated OBIA approach to lineament detection ensures an objective interpre-
185 tation between different visualisations of the data. The resultant lineament populations are examined qualitatively and
186 quantitatively to determine the merits of each operator whilst a semi-automated approach to data quality assessment
187 allows the removal of likely false positive lineaments.

3.1. Feature extraction methods

The operations performed on the data are presented in Figure 2, over the magnified area (illustrated in Figure 1b). This small subset of the study shows the edge of the platform and provides a good comparison of how the filters and transforms perform across this pronounced change in depth. It can be seen from Figure 2a that the magnitude of the gradient filter is effective at dealing with the sharp break in the data but, because it is an edge detector, tends toward highlighting the edges of submerged outcrop blocks, rather than identifying fractures in the bedrock. The magnitude of the Sobel filter is similar in its output due to the subtle difference in its kernel with the magnitude of gradient (Equations 5 and 8), the result in Figure 2b captures edges of blocks and is not well suited to define minima. Although the filtered data range appears to be better at recognising structure in the off-platform data, it is oversaturated on the platform resulting in an apparent loss of resolution.

Compared to the previous filters, the Laplacian filter produces a smoother visualisation of the data. The 3 x 3 kernel shown in Figure 2c provides a slight enhancement on the data to highlight structures but is overall indistinct at this scale and appears to have greater noise. The 5 x 5 kernel (Figure 2d) emphasises more structures in both on-platform and off-platform areas whilst reducing noise to give a sharper image.

Figure 2e displays the hillshade transform for the illumination azimuth of 225° and zenith of 45° that enhances the NW-SE structures in the area. It should be noted that the method also incorporates an orthogonal hillshade at 315° and a 45° zenith to enhance the subordinate NNE-SSW features. The image clearly detects structures in the on-platform areas of the seafloor but struggles to highlight such detail in the deeper off-platform areas. The tilt derivative provides a more complete picture where structures are equally apparent despite the step-change in platform height over the area. The use of a total horizontal derivative in the denominator means that there is no azimuthal bias to highlight particular orientations of lineaments in the data, as is the case with the hillshade transform.

3.2. Lineament populations

The derived lineaments are presented and discussed with respect to the relative performance of each operator. A visual inspection is presented of a subset of the area (outlined in Figure 1b) is used to provide a visual assessment

212 of the different lineament sets. Statistical analysis is conducted on the whole lineament population for each feature
213 extraction method to explore the data distribution with respect to length, orientation and depth of the lineaments. The
214 complete lineament set for each method can be found in the Supplementary Information.

215 **3.2.1. Data quality assessment**

216 A key aspect of semi-automated lineament detection is identifying where false positive lineaments are being intro-
217 duced into the final product. This can be difficult to quantify in absolute terms without manual inspection of individual
218 lineaments; an onerous task for large datasets. Spurious lineaments can be introduced by either similarity between
219 desirable and undesirable features or due to artefacts in the data. Improved feature extraction methods can assist in
220 correctly targeting desired geological lineaments, however, once introduced, false positive occurrences must be filtered
221 out using either through statistical, geometric or spatial methods.

222 Statistical methods are often easy to apply and can include identifying a threshold in the population at which to
223 discard lineaments. This approach can be crude and is not particularly insightful, often resulting in the removal of
224 genuine data, however, it can also be a question of scale and usability. For example, it is common practise to use
225 Tobler's rule to derive a minimum "map scale" from an image by multiplying the pixel resolution by 2000 (Tobler,
226 1988). In this case, for a 2 m pixel resolution, the minimum map scale is 1:4000 where 1 mm represents 4000 mm
227 (4 metres). Lines of 1 mm length on a map result in data saturation and, for any map, one could argue that mapped
228 lineaments shorter than 4 mm are too detailed. In this study, a 4 mm line at our minimum map scale of 1:4000 would
229 make lineaments shorter than 16 m redundant. Therefore, a threshold has been applied to remove lineaments with
230 lengths less than 16 m. Finally, entries that resulted in anomalous NaN values in the final datasets were removed
231 resulting in 6, 2 and 1 lineaments being removed from the TDR-derived data and the 3 x 3 and 5 x 5 Laplacian filters,
232 respectively; these were likely generated when calculating the average depth of a lineament.

233 Geometric filtering can include looking at shape of the image object and/or its relationship to others. OBIA methods
234 are particularly powerful at geometric filtering due to the combination of vector-type metadata for image objects and
235 the internal raster-based statistics which is enhanced by the topological analysis of different image objects. These have

236 been incorporated into the workflow adopted from Yeomans et al. (2019) where the asymmetry, internal mean and area
237 of image objects are considered as well as their relationship to adjoining image objects. These help to merge adjacent
238 image objects that are similar whilst removing unusual geometries that are likely to not represent true lineaments.

239 Spatial filtering requires a supplementary spatial dataset that can be used to identify co-located features. It can be
240 a particularly effective method over onshore areas for removing lineaments that pertain to roads or field boundaries,
241 should these data be readily available, however such datasets are less prevalent in offshore areas. Creating masks from
242 the original bathymetric data can provide an efficient spatial filter for identifying likely false positive lineaments. In this
243 study, smooth areas of the seabed were interpreted as sediment cover obscuring potential seafloor lineaments. These
244 areas can be identified by deriving a textural Terrain Ruggedness Index (TRI) raster layer from the original bathymetric
245 model, where smooth areas (low values) can be selected using a threshold to highlight likely areas of sediment cover.
246 The resulting mask can then be used to post-process lineament datasets and remove likely false positive lineaments in
247 these areas. The threshold is user-defined and requires careful consideration so as not to mask viable areas but provides
248 an efficient means of removing likely spurious data. The full mask for this study is presented in the Supplementary
249 Information.

250 By applying the spatial filter using the TRI mask to the lineament data across the whole study area, lineaments
251 were removed over these potentially problematic areas for each method; precise numbers are given in Table 1. Due
252 to the mask covering areas largely in off-platform areas, the greatest number of lineaments were selected from the
253 TDR-derived population. However, it is worth noting that comparatively few lineaments were detected in off-platform
254 areas for the other operators.

255 **3.2.2. Visual lineament assessment**

256 The six lineament sets derived from different feature extraction methods are displayed in Figure 3. These highlight
257 the performance of each operator from on-platform to off-platform areas, where the water depth increases >10 metres.
258 The off-platform area has some sedimentary cover producing low-quality data but does display NW-SE structures that
259 correlate with on-platform structures.

260 The number of lineaments derived from gradient-filtered data across Zone 1 is not substantial, with the majority
261 of lineaments found over on-platform areas. Figure 3a weakly defines some NW-SE features in the data but the lack
262 of contiguous segments make interpretation more difficult. The off-platform areas perform even more poorly and
263 this is likely a function of the lack of smoothing (as mentioned for Zone 2) but also the more subtle features in off-
264 platform areas being masked by the significant gradient caused across the step in the seafloor. In Figure 3b, lineaments
265 derived from Sobel-filtered data show a reasonable level of detail in the on-platform areas although continuous features
266 are difficult to observe. The off-platform areas are an improvement with respect to the gradient methods but also lack
267 easily identifiable structures. Despite the smoothing component incorporated into the Sobel kernels, these off-platform
268 lineaments remain elusive.

269 Lineaments derived from Laplacian-filtered data show reasonable on-platform features. The 3 x 3 kernel (Figure 3c)
270 identifies an abundance of short lineaments, although these produce short segments that do not easily define NW-SE
271 or NNE-SSW trending structures. The off-platform lineaments appear to be largely a function of noise, not giving
272 clear definition to any features, and are considered false positives. In contrast, the 5 x 5 kernel (Figure 3d) produces a
273 less noisy lineament population and longer lineament segments, clearly defining some key structures in Zone 1. The
274 off-platform areas, however, do not display any distinguishable features. The interpretation that the 5 x 5 kernel has
275 been effective at suppressing noisy lineaments further suggests off-platform lineaments detected using data filtered by
276 the 3 x 3 kernel are spurious.

277 A vast population of lineaments across the on-platform area has been generated from the hillshade-transformed
278 data (Figure 3e). Major NW-SE structures are clearly identified and are traceable with long segment lengths to the
279 lineaments. The population also contains a significant amount of small lineaments which appear to be more robust
280 when compared with the noisier populations seen in Figure 3c from the 3 x 3 Laplacian filter. However, the off-platform
281 area underperforms, showing few lineaments and many of those that are detected do not have contiguous segments. In
282 contrast, lineaments derived from the TDR-transformed data show clear structures, albeit with fewer short segments in
283 some areas (Figure 3f). The lineaments detected define clear NW-SE trending features in on-platform areas and also
284 identify some subordinate NNE-SSW structures. Importantly, the off-platform areas show an abundance of lineaments,

285 which present contiguous segments, and are traceable back to on-platform features; although, many are generated in
286 areas of sediment cover which could be the result of amplified noise.

287 3.2.3. *Lineament analysis*

288 A statistical analysis of the lineaments for each feature extraction method over the whole study area are presented
289 in Table 1. These describe the mean, standard deviation and median of each lineament population as well as the
290 range, skewness and kurtosis for lineament lengths and their approximate depth. The number of observations for each
291 extraction method is also listed where a clear distinction can be made between the number of lineaments derived from
292 transformed data versus filtered data where the hillshade transform identifies the highest number of lineaments.

293 Lengths for each extraction method all show a strong positive skew and high kurtosis, characteristic of populations
294 where more short lineaments are identified over larger ones. This indicates that the mean is not as reliable a metric and
295 the median should be used. Shorter median lineament lengths are detected by the gradient and Sobel directional filters
296 and this is reflected in their range. The Laplacian filters provide good lineament lengths, comparable to the hillshade
297 and TDR transform but the 3 x 3 kernel produces a large amount of lineaments but never >100 m. Equally, the 5 x 5
298 kernel produces the third lowest number of lineaments whilst having a high standard deviation indicating a small but
299 varied population. The hillshade and TDR transform operators perform well produce large lineament populations, at
300 good median lengths with the largest ranges.

301 The depth values are calculated by assigning the point value from the bathymetric data at the centroid of the polyline
302 in the vector data where the centroid is assumed to approximate the midpoint of the lineament. The depth data generally
303 show a more Gaussian distribution represented by skewness values close to zero, albeit more flattened as seen by the
304 low kurtosis. Therefore, in contrast to lineament lengths, the mean is a more reliable metric for identifying the average
305 depths at which lineaments are sensed. The hillshade transform and the Laplacian, Sobel and gradient-based filters
306 show a fairly consistent picture of the depths at which lineaments are identified but there is a marked difference in the
307 depth at which lineaments are detected for the TDR transform, which clearly shows a greater mean depth and higher
308 standard deviation. This is further illustrated by the kernel density estimation in Figure 4 where the TDR shows a
309 distinctly different shape at depths deeper than -28 m (i.e. off-platform areas). It can be seen that between depths of

310 -28 m and 0 m the trend in lineament density is similar for all methods, however, the large population of lineaments
311 noted for the 5 x 5 Laplacian kernel in Table 1 is focused between depths of -16 m to -20 m. The KDE function shows
312 relative density of lineaments, thus, the lower values within this range for the TDR transform do not represent fewer
313 lineaments at these depths but demonstrate that the method captures lineaments across the depth range.

314 Axial data for lineaments derived for each method have been calculated and presented in rose diagrams in Figure 5.
315 These have been prepared using equal-area wedge rose plots following the guidelines presented by Sanderson and
316 Peacock (2020). Bin sizes are suggested to be calculated by dividing the range (180° for axial data) by the number of
317 observations to the nearest 5° . Due to the large population sizes this resulted in values $\ll 1^\circ$; in this case a bin size of
318 5° intervals was selected.

319 The rose diagram for the directional gradient-based feature extraction method (Figure 5a) is clearly aligned to the
320 two axes upon which the directions were selected and clearly highlights the orientation of major NW-SE and subor-
321 dinate minor NNE-SSW structures. The Sobel filter (Figure 5b), where the directional components were aligned N-S
322 and E-W captures both orientations of features, but displays greater variation about these directions, particularly in the
323 NW-SE axis. The Laplacian filters present quite a different population of lineament orientations being detected. The
324 3 x 3 kernel (Figure 5c) captures a strong NNW-SSW component of equal magnitude to the major NW-SE structures
325 whereas the 5 x 5 kernel in Figure 5d presents a more consistent picture of major NW-SE and subordinate NNE-SSW
326 features. The likely explanation for the discrepancies between the two kernels is, whilst both are second order deriva-
327 tives and more sensitive to noise, the 5 x 5 kernel allows more smoothing compared to the 3 x 3 kernel which struggles
328 to mitigate noisy data. The rose diagram of the hillshade transform (Figure 5e) highlights the major NW-SE trend
329 strongly with little variation other than a subordinate NNE-SSW trend which is strongly aligned perpendicular to the
330 orthogonal hillshade azimuth. The TDR transform produces a range of lineaments, with a strong NW-SE population,
331 however, the subordinate NNE-SSW trend is either underrepresented or skewed more towards the NNE-SSW orienta-
332 tion observed in the 3 x 3 Laplacian filter. Interestingly, this NNE trend is present in all lineament populations apart
333 from the hillshade method where it is clearly absent.

334 3.3. The effect of false positive results

335 The data quality assessment using the TRI identified areas sediment cover assuming these remain smooth and free
336 of artefacts. By using these areas as a mask, likely spurious lineaments can be spatially filtered and removed as false
337 positive results. Due to the low numbers of selected lineaments for all methods apart from the TDR transform, only the
338 TDR-derived lineaments are used here to analyse the effects of false positives on the population. The total number of
339 false positives removed from spatial filtering from the TDR-derived dataset was 549 (Table 1). These are presented and
340 compared to the remaining lineament population in Figure 6 where equal-area wedge rose diagrams are implemented.

341 A rose diagram of the unfiltered data is shown in Figure 6a where a strong modal axis can be identified in both a NW-
342 SE and NNE-SSW orientation. Figure 6b shows a strong modal axis approximately NNE-SSW and are concentrated
343 over areas that were interpreted as sediment-covered due to their smoothness when applying the TRI mask. The TDR
344 transform is often heralded for its ability to give equal weight to minor features on a surface whilst in the presence of
345 larger structures ((Miller and Singh, 1994; Verduzco et al., 2004), however, the strong population in this orientation is
346 likely caused by small artefacts that are exaggerated by the TDR transform. We therefore suggest caution when using
347 the TDR transform in areas of sediment cover. Furthermore, the rose plot of data generated by the 3 x 3 kernel of the
348 Laplacian filter in Figure 5c shows a similarly strong NNE-SSW trend which may imply that similar artefacts are being
349 identified by this filter but are not found of areas of sediment cover.

350 By conducting an assessment of these potentially spurious lineaments, it an oversampling of NNE-oriented linea-
351 ments can be demonstrated. Removing these from the population results in a more representative set of lineaments
352 where a subordinate NNE-SSW trend is comparable with the original study of Nixon et al. (2012). Whether these false
353 positive results are due to small sand waves upon the sediment cover, or whether they represent artefacts caused by
354 the interaction with unconsolidated substrate is unclear. The identification of areas that do not represent submerged
355 outcrop determines that the source is not geological. The strong modal axis identified in the 3 x 3 Laplacian filter, and
356 the susceptibility of the filter to noise, may indicate a sonic source but further investigation is beyond the scope of this
357 study.

358 3.4. Comparison of methods

359 The different feature extraction techniques tested in this study show markedly different lineament populations that
360 are variably affected by the sharp break in the seafloor. Gradient-based filters are the least effective, despite the initial
361 kernels being selected to emphasise NW and NE gradients and the rose diagrams show that the directional filtering has
362 forced the lineament population towards these major trends. The Sobel filter underperforms, relative to other methods,
363 even with smoothing incorporated into the kernel but does allow greater flexibility away from the major modal axes.
364 Neither of these gradient-based filters are capable of capturing lineaments in the off-platform areas.

365 The Laplacian filters successfully identify structures, albeit discontinuously, with a distinct improvement when
366 using the 5 x 5 kernel. Despite reasonable success on the platform, the filters fail to capture any significant structure
367 in the off-platform area. The azimuth-invariant nature of these kernels is demonstrated in the rose diagrams where
368 major NW-SE faults are still readily identified as a modal axis, but with greater contributions from the subordinate
369 NNE-SSW trend. These Laplacian filters are second-order derivatives and sensitive to noise, which may be manifest
370 in the 3 x 3 kernel where a NNE-SSW modal axis dominates (Figure 5c). In comparison, the 5 x 5 kernel does not
371 capture this, which may be a function of greater smoothing over the larger kernel.

372 Numerous, clear NW-SE lineaments are identified when using the hillshade transform in on-platform areas. The
373 transform is the most prolific with nearly 8000 lineaments being identified despite being processed to only focus on
374 NW-SE trends, as evidenced by the rose diagram in Figure 5b. Including another hillshade with an orthogonal azimuth
375 (e.g. Scheiber et al., 2015) or taking a multi-hillshade clustering approach (e.g. Šilhavý et al., 2016) would likely further
376 improve this analysis. Unfortunately, off-platform areas do not capture features to the same level of consistency and
377 are not easily interpretable.

378 The TDR transform captures the two major NW-SE and NNE-SSW trends in the area and produced the second
379 largest lineament population, with good lineament lengths. It also was the most effective operator for detecting linea-
380 ments in both on- and off-platform areas across the break in the seafloor. This is due to the inclusion of the vertical
381 derivative that provides a normalisation to vertical changes across the study area. However, the transform is potentially

382 fallible if not applied with care to identify false positive lineaments. Due to the sensitivity of the algorithm, and the
383 equal weighting of large and small lineaments, spurious lineaments are produced over areas interpreted as sediment
384 cover and are thus do not represent a geological lineament. Spatial filtering, using a TRI layer, can efficiently remove
385 these false positive lineaments from the population and return a more realistic subset of detected lineaments.

386 Segmented lineaments are common across all analyses and may be a reflection of slight changes in fault properties
387 along strike (e.g. damage zones) that may have preferentially eroded in the seafloor. Thus, post-processing to link these
388 segments should be investigated (e.g. topological methods such as Panagiotakis and Kokinou, 2015). Furthermore,
389 the possible detection of amplified noise in some off-platform areas by the TDR transform could be mitigated by
390 prior application of a smoothing filter. Despite this, the TDR transform is still considered to be the best operators for
391 lineament detection where a sharp break in slope is present in the source data.

392 4. Conclusions

393 Six different operators have been tested as feature extraction tools prior to semi-automated lineament detection. The
394 different filters and transforms have been assessed based on their performance to detect lineaments from bathymetric
395 data where step-changes (palaeocoastlines) in the seafloor platform are present. These included the magnitude of
396 gradient through combined NW and NE gradient filters, the magnitude of the Sobel filter, two Laplacian filters (3 x 3
397 and a 5 x 5 kernels) as well as the hillshade and TDR transform.

398 The bathymetric data used in this study show a network of NW-SE and NNE-SSW faults sets that can be identified
399 using semi-automated lineament detection techniques. Semi-automated approaches have been demonstrated to produce
400 markedly different lineament populations based on different feature extraction tools. Thus, testing over a small area is
401 an important step prior to using semi-automated methods on regional scale.

402 The semi-automated OBIA lineament detection method of Yeomans et al. (2019) has been applied to bathymetric
403 data to analyse the six operators, of which, the TDR transform was most successful. The algorithm also performed well

404 when applied to the hillshade transform, demonstrating the potential to greatly extend the use of the algorithm to analyse
405 other geospatial datasets. The study is noteworthy for developers of future semi-automated lineament algorithms and
406 careful consideration of the feature extraction methods implemented and their potential to generate false positives
407 through noise.

408 The TDR transform is considered to be the most effective operator for identifying lineaments. This study has
409 demonstrated that the use of the TDR transform enhances the data so that abrupt changes in the bathymetry, such
410 as palaeocoastlines, are not detrimental to the analysis. In turn, this increases the area available for interpretation of
411 offshore fault zones. Whilst the resulting lineament population contains longer lineament segments than the other
412 operators, it is worth noting that the TDR transform is not a panacea for lineament detection techniques. For example,
413 subtle artefacts in the data over sediment-covered areas have been amplified and mapped as lineaments. These required
414 careful post-processing using a semi-automated spatial filter based on the texturally-derived TRI. Nevertheless, the
415 TDR transform provides an excellent tool for generating meaningful lineament populations across large studies areas
416 that may contain significant changes in elevation.

417 **Acknowledgements**

418 We thank Camilla Palmiotto and an anonymous reviewer for constructive comments that enhanced this manuscript.
419 CMY is funded by a NERC Highlights grant (NE/S003886/1) on the GWatt project. MH is supported by a NERC
420 GW4+ Doctoral Training Partnership studentship (NE/L002434/1). JLL holds a Vice-Chancellor Scholarship at the
421 University of Exeter. The data used in this study have been sourced from the UK Hydrographic Office and accessed
422 via the Admiralty Marine Data Portal. The British Geological Survey is thanked for making the BGS Geology 625k
423 (DiGMapGB-625) data freely available. Dr Matt Hall is kindly thanked for his insights into some of the nuances of
424 QGIS and color ramps. The Software Underground community is also thanked for their assistance deciphering Python
425 errors.

References

- 426
427 Airo, M.L., 2013. Structural interpretation of airborne geophysical data: examples from Finland. Technical Report. Geologian Tutkimuskeskus
428 (GTK). Espoo.
- 429 Airo, M.L., Wennerström, M., 2010. Application of regional aeromagnetic data in targeting detailed fracture zones. *Journal of Applied Geophysics*
430 71, 62–70. URL: <http://linkinghub.elsevier.com/retrieve/pii/S0926985110000388>, doi:10.1016/j.jappgeo.2010.03.003.
- 431 Al-Azemi, A.M., Divi, R., 2017. Extraction of Geological Structural Lineaments in Northern Kuwait Using High Resolution Landsat 8 ETM+
432 Satellite Images and Edge Enhancement Techniques. *Journal of Engineering Sciences and Information Technology* 1, 18–35.
- 433 Andrews, B.J., Roberts, J.J., Shipton, Z.K., Bigi, S., Tartarello, M.C., Johnson, G., 2019. How do we see fractures? Quantifying subjective
434 bias in fracture data collection. *Solid Earth* 10, 487–516. URL: <https://www.solid-earth.net/10/487/2019/>, doi:10.5194/
435 se-10-487-2019.
- 436 Ault, A.K., Frenzel, M., Reiners, P.W., Woodcock, N.H., Thomson, S.N., 2016. Record of paleofluid circulation in faults revealed by hematite(U-
437 Th)/He and apatite fission-track dating: An example from Gower Peninsula fault fissures, Wales. *Lithosphere* 8, 379–385. doi:10.1130/L522.1.
- 438 Blaschke, T., Burnett, C., Pekkarinen, A., 2004. Image Segmentation Methods for Object-based Analysis and Classification, in: de Jong, S.M.,
439 van der Meer, F.D. (Eds.), *Remote Sensing Image Analysis: Including the Spatial Domain*. Springer Netherlands, pp. 211–236.
- 440 Canny, J., 1986. A computational approach to edge detection. *IEEE Transactions on Pattern Analysis and Machine Intelligence* 8.
- 441 Chapman, T.J., 1989. The Permian to Cretaceous structural evolution of the Western Approaches Basin (Melville sub-basin), UK. *Geological*
442 *Society Special Publication* 44, 177–200. doi:10.1144/GSL.SP.1989.044.01.11.
- 443 Cheadle, M.J., McGeary, S., Warner, M.R., Matthews, D.H., 1987. Extensional structures on the western UK continental shelf: A review of evidence
444 from deep seismic profiling. *Geological Society Special Publication* 28, 445–465. doi:10.1144/GSL.SP.1987.028.01.28.
- 445 Collier, J.S., Gupta, S., Potter, G., Palmer-Felgate, A., 2006. Using bathymetry to identify basin inversion structures on the English Channel
446 shelf. *Geology* 34, 1001. URL: <https://pubs.geoscienceworld.org/geology/article/34/12/1001-1004/129412>, doi:10.1130/
447 G22714A.1.
- 448 Davies, E.R., 1986. Constraints on the design of template masks for edge detection. *Pattern Recognition Letters* 4, 111–120. doi:10.1016/
449 0167-8655(86)90032-2.
- 450 Fairhead, J.D., Mackenzie, C., Green, C.M., Verduzco, B., 2004. A new set of magnetic field derivatives for mapping mineral prospects.
451 ASEG Extended Abstracts 2004, 1–4. URL: <https://www.tandfonline.com/doi/full/10.1071/ASEG2004ab042>, doi:10.1071/
452 ASEG2004ab042.
- 453 Favalli, M., Fornaciari, A., 2017. Visualization and comparison of DEM-derived parameters. Application to volcanic areas. *Geomorphology* 290,
454 69–84. URL: <http://dx.doi.org/10.1016/j.geomorph.2017.02.029>, doi:10.1016/j.geomorph.2017.02.029.
- 455 Grebby, S., Cunningham, D., Naden, J., Tansey, K., 2012. Application of airborne LiDAR data and airborne multispectral imagery to struc-
456 tural mapping of the upper section of the Troodos ophiolite, Cyprus. *International Journal of Earth Sciences* 101, 1645–1660. doi:10.1007/
457 s00531-011-0742-3.
- 458 Han, L., Liu, Z., Ning, Y., Zhao, Z., 2018. Extraction and analysis of geological lineaments combining a DEM and remote sensing images from the
459 northern Baoji loess area. *Advances in Space Research* 62, 2480–2493. URL: <https://doi.org/10.1016/j.asr.2018.07.030>, doi:10.
460 1016/j.asr.2018.07.030.
- 461 Hashim, M., Ahmad, S., Johari, M.A.M., Pour, A.B., 2013. Automatic lineament extraction in a heavily vegetated region using Landsat Enhanced
462 Thematic Mapper (ETM+) imagery. *Advances in Space Research* 51, 874–890. URL: <http://dx.doi.org/10.1016/j.asr.2012.10.004>,
463 doi:10.1016/j.asr.2012.10.004.
- 464 Hell, B., Broman, B., Jakobsson, L., Jakobsson, M., Magnusson, Å., Wiberg, P., 2012. The use of bathymetric data in society and science: A review
465 from the Baltic Sea. *Ambio* 41, 138–150. doi:10.1007/s13280-011-0192-y.
- 466 Hillis, R.R., Holford, S.P., Green, P.F., Doré, A.G., Gatliff, R.W., Stoker, M.S., Thomson, K., Turner, J.P., Underhill, J.R., Williams, G.A.,
467 2008. Cenozoic exhumation of the southern British Isles. *Geology* 36, 371–374. URL: [https://pubs.geoscienceworld.org/geology/
468 article/36/5/371-374/29723](https://pubs.geoscienceworld.org/geology/article/36/5/371-374/29723), doi:10.1130/G24699A.1.
- 469 Höfle, B., Rutzinger, M., 2011. Topographic airborne LiDAR in geomorphology: A technological perspective. *Zeitschrift für Geomorphologie* 55,
470 1–29. doi:10.1127/0372-8854/2011/0055S2-0043.
- 471 Holder, M.T., Leveridge, B.E., 1986. A model for the tectonic evolution of south Cornwall. *Journal of the Geological Society, London* 143, 125–134.
472 doi:10.1144/gsjgs.143.1.0125.
- 473 Holloway, S., Chadwick, R.A., 1986. The Sticklepath-Lustleigh fault zone: Tertiary sinistral reactivation of a Variscan dextral strike-slip fault.
474 *Journal of the Geological Society, London* 143, 447–452.
- 475 Kokinou, E., Panagiotakis, C., 2018. Structural pattern recognition applied on bathymetric data from the Eratosthenes Seamount (Eastern Mediter-
476 ranean, Levantine Basin). *Geo-Marine Letters* 38, 527–540. doi:10.1007/s00367-018-0553-7.
- 477 Lang, S., 2008. Object-based image analysis for remote sensing application: modeling reality - dealing with complexity, in: Blaschke, T., Lang, S.,
478 Hay, G.J. (Eds.), *Object-Based Image Analysis: Spatial Concepts for Knowledge-Driven Remote Sensing Applications*. Springer-Verlag, Berlin,
479 pp. 3–27.
- 480 Leveridge, B.E., Hartley, A.J., 2006. The Variscan Orogeny: the development and deformation of Devonian/Carboniferous basins in SW England and
481 South Wales, in: Brenchley, P.J., Rawson, P.F. (Eds.), *The Geology of England and Wales*. 2nd ed.. The Geological Society, London. chapter 10,
482 pp. 225–256.
- 483 Leveridge, B.E., Holder, M.T., Goode, A.J.J., Scrivener, R.C., Jones, N.S., Merriman, R.J., 2002. Geology of the Plymouth and south-east Cornwall
484 area. *Memoir of the British Geological Survey, Sheet 348*. England and Wales.
- 485 Lloyd, G.E., Chinnery, N., 2002. The Bude Formation, SW England - three-dimensional, intra-formational Variscan imbricate stack? *Journal of*
486 *Structural Geology* 24, 1259–1280.
- 487 Maini, R., Aggarwal, H., 2009. Study and comparison of various image edge detection techniques. *International Journal of Image Processing* 3, 1–11.
488 doi:<http://www.doaj.org/doaj?func=openurl&genre=article&issn=19852304&date=2009&volume=3&issue=1&page=1>.

- 489 Mallast, U., Gloaguen, R., Geyer, S., Rödiger, T., Siebert, C., 2011. Derivation of groundwater flow-paths based on semi-automatic extraction of
490 lineaments from remote sensing data. *Hydrology and Earth System Sciences* 15, 2665–2678. doi:10.5194/hess-15-2665-2011.
- 491 Marpu, P.R., Niemeier, I., Nussbaum, S., Gloaguen, R., 2008. A procedure for automatic object-based classification, in: Blaschke, T., Lang, S.,
492 Hay, G.J. (Eds.), *Object-Based Image Analysis: Spatial Concepts for Knowledge-Driven Remote Sensing Applications*, pp. 169–184. doi:10.
493 1007/978-3-540-77058-9.
- 494 Marr, D., Hildreth, E., 1980. Theory of edge detection. *Proceedings of the Royal Society of London. Series B. Biological Sciences* 207, 187–217.
495 URL: <https://royalsocietypublishing.org/doi/10.1098/rspb.1980.0020>, doi:10.1098/rspb.1980.0020.
- 496 Mavrantza, O.D., Argialas, D.P., 2006. Object-oriented image analysis for the identification of geologic lineaments. *International Archives of*
497 *Photogrammetry, Remote Sensing and Spatial Information Sciences* 36, 1–6.
- 498 Middleton, M., Schnur, T., Sorjonen-ward, P., Hyvönen, E., 2015. Geological lineament interpretation using the Object-Based Image Analysis
499 Approach: results of semi-automated analyses versus visual interpretation. *Geological Survey of Finland, Special Paper* 57, 135–154.
- 500 Miller, H.G., Singh, V., 1994. Potential field tilt - a new concept for location of potential field sources. *Journal of Applied Geophysics* 32, 213–217.
501 doi:10.1016/0926-9851(94)90022-1.
- 502 Moore, G.K., Waltz, F.A., 1983. Objective procedures for lineament enhancement and extraction (Eros Data Center). *Photogrammetric Engineering*
503 *& Remote Sensing* 49, 641–647.
- 504 Morris, K., 1991. Using knowledge-base rules to map the three-dimensional nature of geological features. *Photogrammetric Engineering & Remote*
505 *Sensing* 57, 1209–1216.
- 506 Mwaniki, M.W., Moeller, M.S., Schellmann, G., 2015. A comparison of Landsat 8 (OLI) and Landsat 7 (ETM+) in mapping geology and visualising
507 lineaments: A case study of central region Kenya. *International Archives of the Photogrammetry, Remote Sensing and Spatial Information*
508 *Sciences - ISPRS Archives* 40, 897–903. doi:10.5194/isprsarchives-XL-7-W3-897-2015.
- 509 Nixon, C.W., Sanderson, D.J., Bull, J.M., 2012. Analysis of a strike-slip fault network using high resolution multibeam bathymetry, offshore
510 NW Devon U.K. *Tectonophysics* 541-543, 69–80. URL: <http://dx.doi.org/10.1016/j.tecto.2012.03.021>, doi:10.1016/j.tecto.
511 2012.03.021.
- 512 Nyberg, B., Nixon, C.W., Sanderson, D.J., 2018. NetworkGT: A GIS tool for geometric and topological analysis of two-dimensional fracture
513 networks. *Geosphere* 14, 1618–1634. doi:10.1130/GES01595.1.
- 514 Panagiotakis, C., Kokinou, E., 2015. Linear pattern detection of geological faults via a topology and shape optimization method. *IEEE Journal of*
515 *Selected Topics in Applied Earth Observations and Remote Sensing* 8, 3–11. doi:10.1109/JSTARS.2014.2363080.
- 516 Power, H.E., Clarke, S.L., 2019. 3D seismic-derived bathymetry: a quantitative comparison with multibeam data. *Geo-Marine Letters* 39, 447–467.
517 doi:10.1007/s00367-019-00596-w.
- 518 Rahnama, M., Gloaguen, R., 2014. TecLines: A MATLAB-Based Toolbox for Tectonic Lineament Analysis from Satellite Images and DEMs,
519 Part 1: Line Segment Detection and Extraction. *Remote Sensing* 6, 5938–5958. URL: <http://www.mdpi.com/2072-4292/6/7/5938>,
520 doi:10.3390/rs6075938.
- 521 Rattey, P.R., Sanderson, D.J., 1984. The structure of SW Cornwall and its bearing on the emplacement of the Lizard Complex. *Journal of the*
522 *Geological Society, London* 141, 87–95.
- 523 Rutzinger, M., Höfle, B., Pfeifer, N., Geist, T., Stötter, H., 2006. Object based analysis of airborne laser scanning data for natural hazard purposes
524 using open source components, in: *1st International Conference on Object-based Image Analysis*, p. 5.
- 525 Sanderson, D.J., Dix, J.K., Westhead, K.R., Collier, J.S., 2017. Bathymetric mapping of the coastal and offshore geology and structure of the
526 Jurassic Coast, Weymouth Bay, UK. *Journal of the Geological Society* 174, 498–508. URL: [http://jgs.lyellcollection.org/lookup/](http://jgs.lyellcollection.org/lookup/doi/10.1144/jgs2016-070)
527 doi/10.1144/jgs2016-070, doi:10.1144/jgs2016-070.
- 528 Sanderson, D.J., Peacock, D.C., 2020. Making rose diagrams fit-for-purpose. *Earth-Science Reviews* 201, 103055. URL: [https://](https://doi.org/10.1016/j.earscirev.2019.103055)
529 doi.org/10.1016/j.earscirev.2019.103055<https://linkinghub.elsevier.com/retrieve/pii/S001282521930594X>, doi:10.
530 1016/j.earscirev.2019.103055.
- 531 Scheiber, T., Fredin, O., Viola, G., Jarna, A., Gasser, D., Łapińska-Viola, R., 2015. Manual extraction of bedrock lineaments from high-resolution
532 LiDAR data: methodological bias and human perception. *Journal of the Geological Society of Sweden (GFF)* 137, 362–372. doi:10.1080/
533 11035897.2015.1085434.
- 534 Sedrette, S., Rebaï, N., 2016. Automatic extraction of lineaments from Landsat Etm+ images and their structural interpretation: Case Study in
535 Nefza region (North West of Tunisia). *Journal of Research in Environmental and Earth Sciences* 04, 139–145.
- 536 Shail, R.K., Alexander, A.C., 1997. Late Carboniferous to Triassic reactivation of Variscan basement in the western English Channel: evidence
537 from onshore exposures in south Cornwall. *Journal of the Geological Society, London* 154, 163–168. doi:10.1144/gsjgs.154.1.0163.
- 538 Šilhavý, J., Minár, J., Mentlík, P., Sládek, J., 2016. A new artefacts resistant method for automatic lineament extraction using Multi-Hillshade
539 Hierarchic Clustering (MHHC). *Computers & Geosciences* 92, 9–20.
- 540 Smith, M.J., Clark, C.D., 2005. Methods for the visualization of digital elevation models for landform mapping. *Earth Surface Processes and*
541 *Landforms* 30, 885–900. doi:10.1002/esp.1210.
- 542 Smithurst, L.J.M., 1990. Structural remote sensing of south-west England. *Proceedings of the Ussher Society* 7, 236–241.
- 543 Sobel, I., Feldman, G., 1973. A 3x3 Isotropic Gradient Operator for Image Processing. *Pattern Classification and Scene Analysis*, 271–272.
- 544 Sukumar, M., Venkatesan, N., Babu, C.N.K., 2014. A review of various lineament detection techniques for high resolution satellite images. *Inter-*
545 *national Journal of Advanced Research in Computer Science and Software Engineering* 4, 72–78.
- 546 Thiele, S.T., Grose, L., Samsu, A., Mickelthwaite, S., Vollgger, S.A., Cruden, A.R., 2017. Rapid, semi-automatic fracture and contact mapping
547 for point clouds, images and geophysical data. *Solid Earth* 8, 1241–1253. URL: <https://www.solid-earth.net/8/1241/2017/>, doi:10.
548 5194/se-8-1241-2017.
- 549 Tobler, W., 1988. Resolution, Resampling and All That, in: Mounsey, H., Tomlinson, R. (Eds.), *Building Data Bases for Global Science*. Taylor &
550 Francis, London, pp. 129–137.
- 551 Van Den Eeckhaut, M., Kerle, N., Poesen, J., Hervás, J., 2012. Object-oriented identification of forested landslides with derivatives of single

- 552 pulse LiDAR data. *Geomorphology* 173-174, 30–42. URL: [http://dx.doi.org/10.1016/j.](http://dx.doi.org/10.1016/j.geomorph.2012.05.024)
553 [geomorph.2012.05.024](http://dx.doi.org/10.1016/j.geomorph.2012.05.024), doi:10.1016/j.
554 [geomorph.2012.05.024](http://dx.doi.org/10.1016/j.geomorph.2012.05.024).
- 554 Van Den Eeckhaut, M., Poesen, J., Verstraeten, G., Vanacker, V., Moeyersons, J., Nyssen, J., van Beek, L.P., 2005. The effectiveness of hillshade
555 maps and expert knowledge in mapping old deep-seated landslides. *Geomorphology* 67, 351–363. doi:10.1016/j.geomorph.2004.11.001.
556 Verduzco, B., Fairhead, D., Green, C.M., MacKenzie, C., 2004. New insights into magnetic derivatives for structural mapping. *The Meter Reader*
557 , 116–119.
- 558 Westhead, R.K., McCarthy, D.J., Collier, J.S., Sanderson, D.J., 2018. Spatial variability of the Purbeck–Wight Fault Zone—a long-lived tectonic
559 element in the southern UK. *Proceedings of the Geologists' Association* 129, 436–451. URL: [http://dx.doi.org/10.1016/j.pgeola.](http://dx.doi.org/10.1016/j.pgeola.2017.08.005)
560 [2017.08.005](http://dx.doi.org/10.1016/j.pgeola.2017.08.005), doi:10.1016/j.pgeola.2017.08.005.
- 561 Xu, J., Wen, X., Zhang, H., Luo, D., Li, J., Xu, L., Yu, M., 2020. Automatic extraction of lineaments based on wavelet edge detection and
562 aided tracking by hillshade. *Advances in Space Research* 65, 506–517. URL: <https://doi.org/10.1016/j.asr.2019.09.045><https://linkinghub.elsevier.com/retrieve/pii/S0273117719307239>, doi:10.1016/j.asr.2019.09.045.
563 <https://linkinghub.elsevier.com/retrieve/pii/S0273117719307239>, doi:10.1016/j.asr.2019.09.045.
- 564 Yeomans, C.M., Middleton, M., Shail, R.K., Grebby, S., Lusty, P.A.J., 2019. Integrated Object-Based Image Analysis for semi-automated geological
565 lineament detection in southwest England. *Computers & Geosciences* 123, 137–148 [Available Online November 2018]. URL: [https://doi.](https://doi.org/10.1016/j.cageo.2018.11.005)
566 [org/10.1016/j.cageo.2018.11.005](https://doi.org/10.1016/j.cageo.2018.11.005), doi:10.1016/j.cageo.2018.11.005.

567 **List of Figures**

568 1 A) Regional overview of the study area, detailing the primary geological units in SW England B)
 569 Seafloor depth off of Hartland Point, with the rectangle highlighting an area that contains a step-change
 570 in bathymetry (reflecting a palaeocoastline) used to showcase the feature extraction methods and re-
 571 sulting lineament populations. Geology based upon BGS Geology 625k (DiGMapGB-625) data, with
 572 the permission of the British Geological Survey. 25
 573 2 Zoomed area used to showcase different feature extraction methods used in this study. A) magnitude
 574 of gradient filter; B) magnitude of Sobel filter; C) 3 x 3 Laplacian filter; D) 5 x 5 Laplacian filter; E)
 575 hillshade transform; F) tilt derivative (TDR) transform. 26
 576 3 A subset of the semi-automated lineament populations highlighting performance over the platform
 577 edge where the tilt derivative captures the most consistent lineament set. Derived from A) magnitude
 578 of gradient filter; B) magnitude of Sobel filter; C) 3 x 3 Laplacian filter; D) 5 x 5 Laplacian filter; E)
 579 hillshade transform; F) tilt derivative (TDR) transform. 27
 580 4 Kernel Density Estimate (KDE) plot for the depths at which lineaments are sensed for each method
 581 where GRAD = gradient filter; LP3 = 3 x 3 Laplacian; LP5 = 5 x 5 Laplacian; HS = Hillshade and
 582 TDR = tilt derivative. The TDR-derived lineament population shows a clear deviation from others
 583 where lineaments at depths >-28 m are detected for this transform but not other operators. 28
 584 5 Equal-area wedge rose diagrams for lineament populations derived from each feature extraction tech-
 585 nique. The major NW-SE trend is apparent in all plots but with variable clarity. Plots are based on
 586 guidelines by Sanderson and Peacock (2020). 29
 587 6 Three rose diagrams where A) is the original population of lineaments for the TDR transform; B) is the
 588 population of spurious lineaments; C) the final lineament population for the TDR transform following
 589 spatial filtering. 30

Application of the tilt derivative transform to bathymetric data

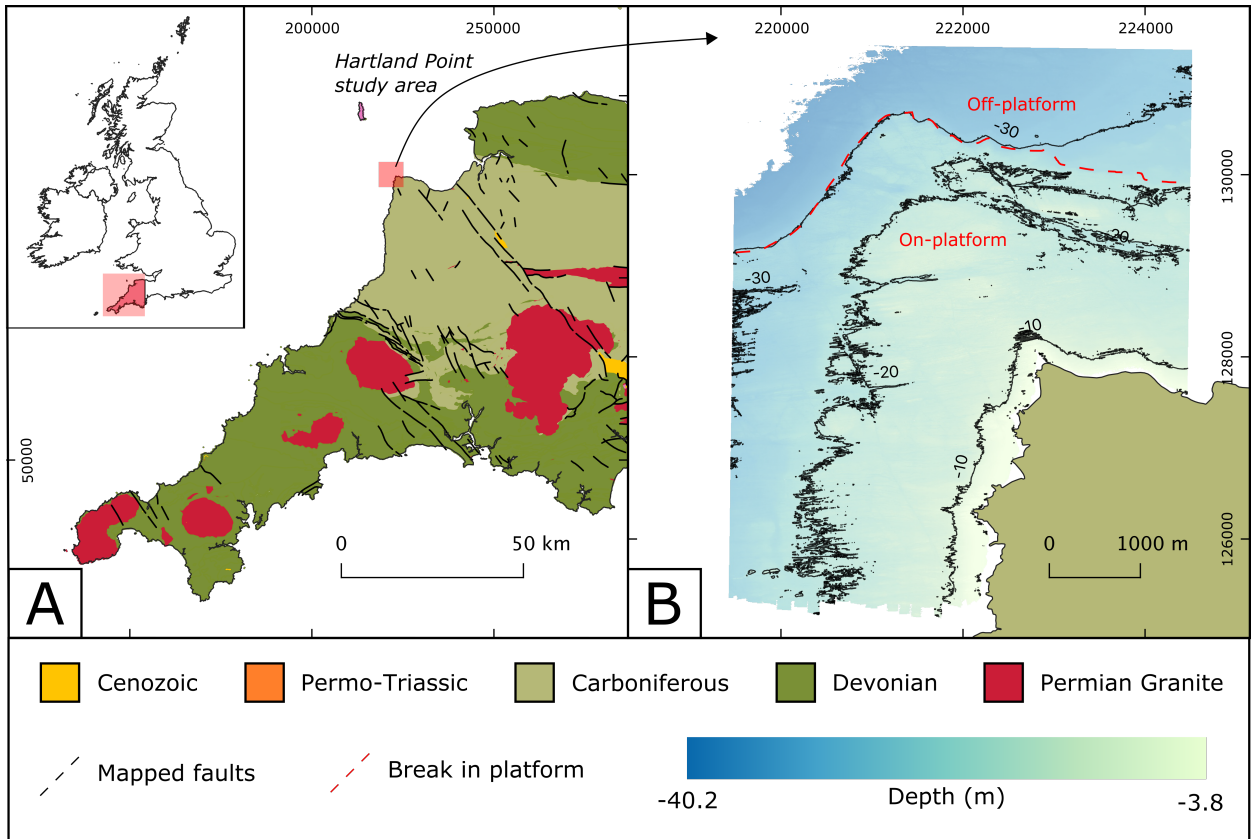


Figure 1: A) Regional overview of the study area, detailing the primary geological units in SW England B) Seafloor depth off of Hartland Point, with the rectangle highlighting an area that contains a step-change in bathymetry (reflecting a palaeocoastline) used to showcase the feature extraction methods and resulting lineament populations. Geology based upon BGS Geology 625k (DiGMapGB-625) data, with the permission of the British Geological Survey.

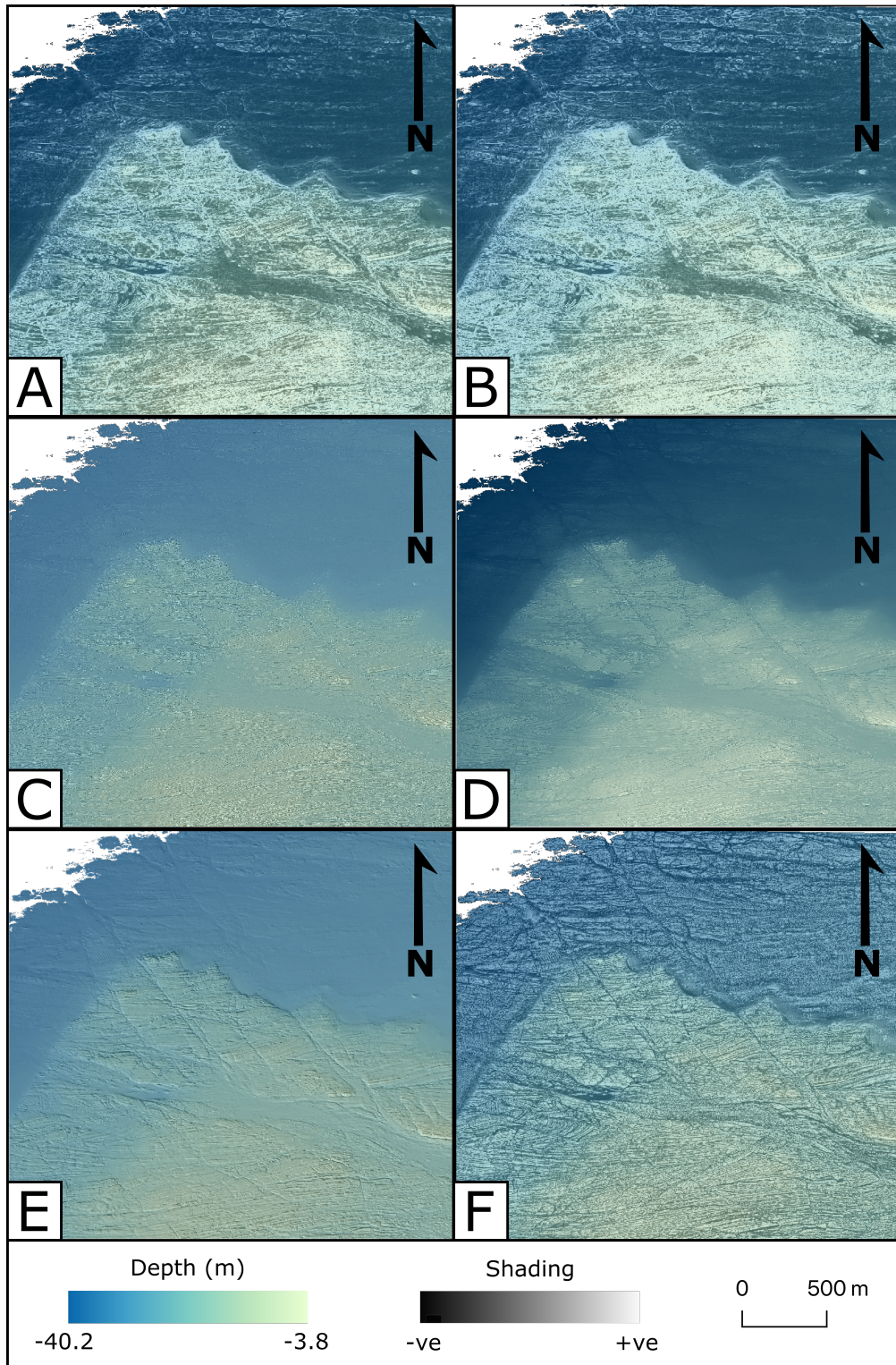


Figure 2: Zoomed area used to showcase different feature extraction methods used in this study. A) magnitude of gradient filter; B) magnitude of Sobel filter; C) 3×3 Laplacian filter; D) 5×5 Laplacian filter; E) hillshade transform; F) tilt derivative (TDR) transform.

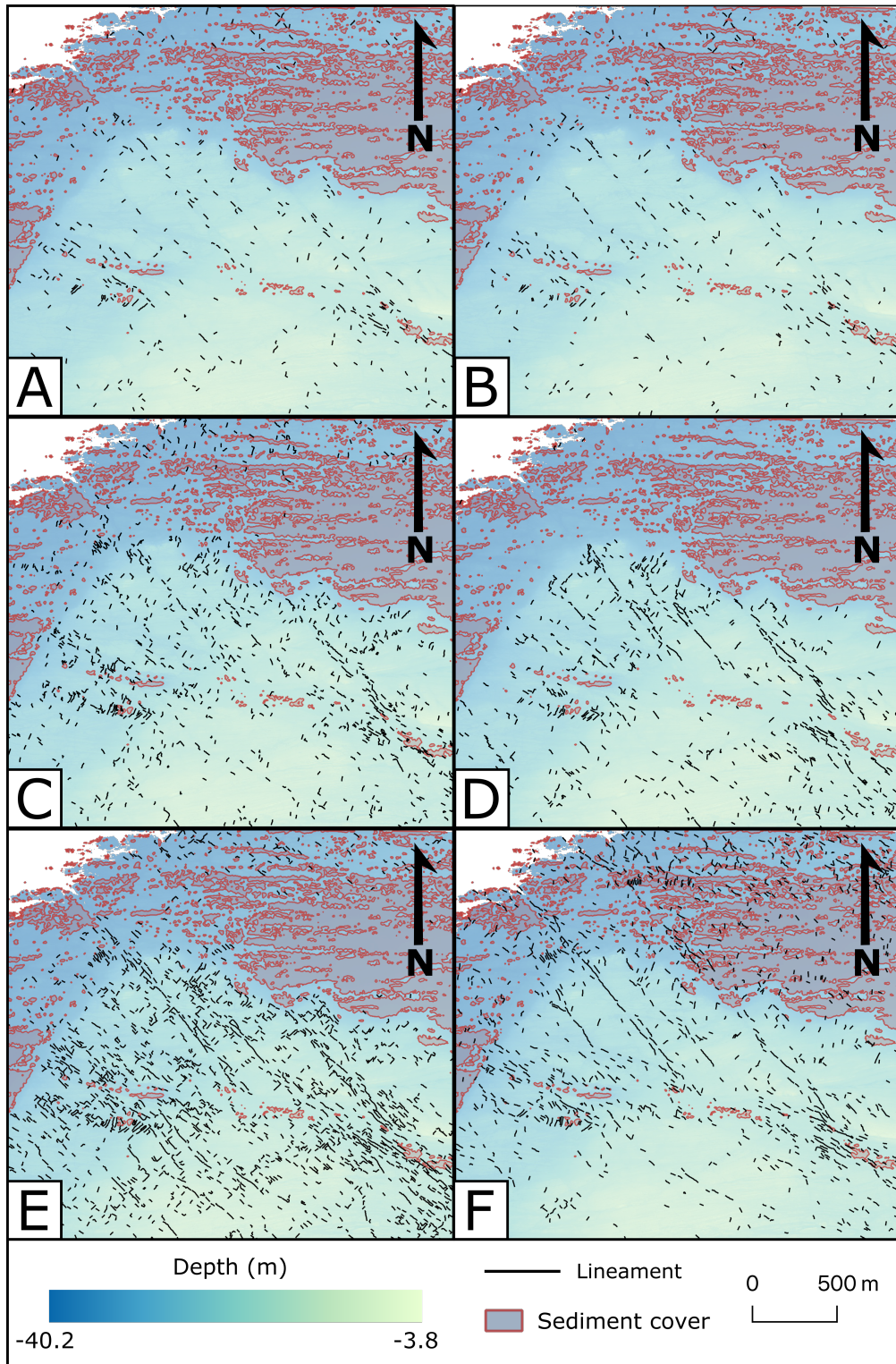


Figure 3: A subset of the semi-automated lineament populations highlighting performance over the platform edge where the tilt derivative captures the most consistent lineament set. Derived from A) magnitude of gradient filter; B) magnitude of Sobel filter; C) 3×3 Laplacian filter; D) 5×5 Laplacian filter; E) hillshade transform; F) tilt derivative (TDR) transform.

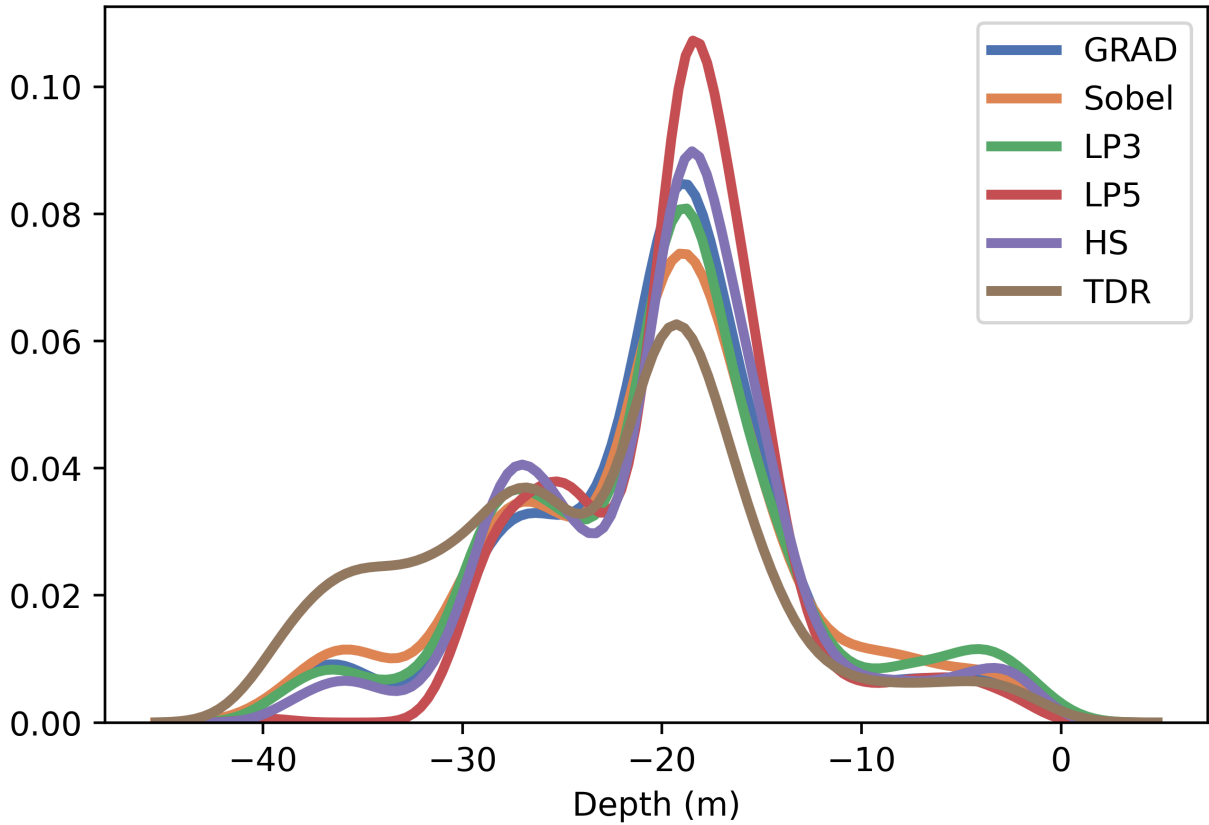


Figure 4: Kernel Density Estimate (KDE) plot for the depths at which lineaments are sensed for each method where GRAD = gradient filter; LP3 = 3×3 Laplacian; LP5 = 5×5 Laplacian; HS = Hillshade and TDR = tilt derivative. The TDR-derived lineament population shows a clear deviation from others where lineaments at depths > -28 m are detected for this transform but not other operators.

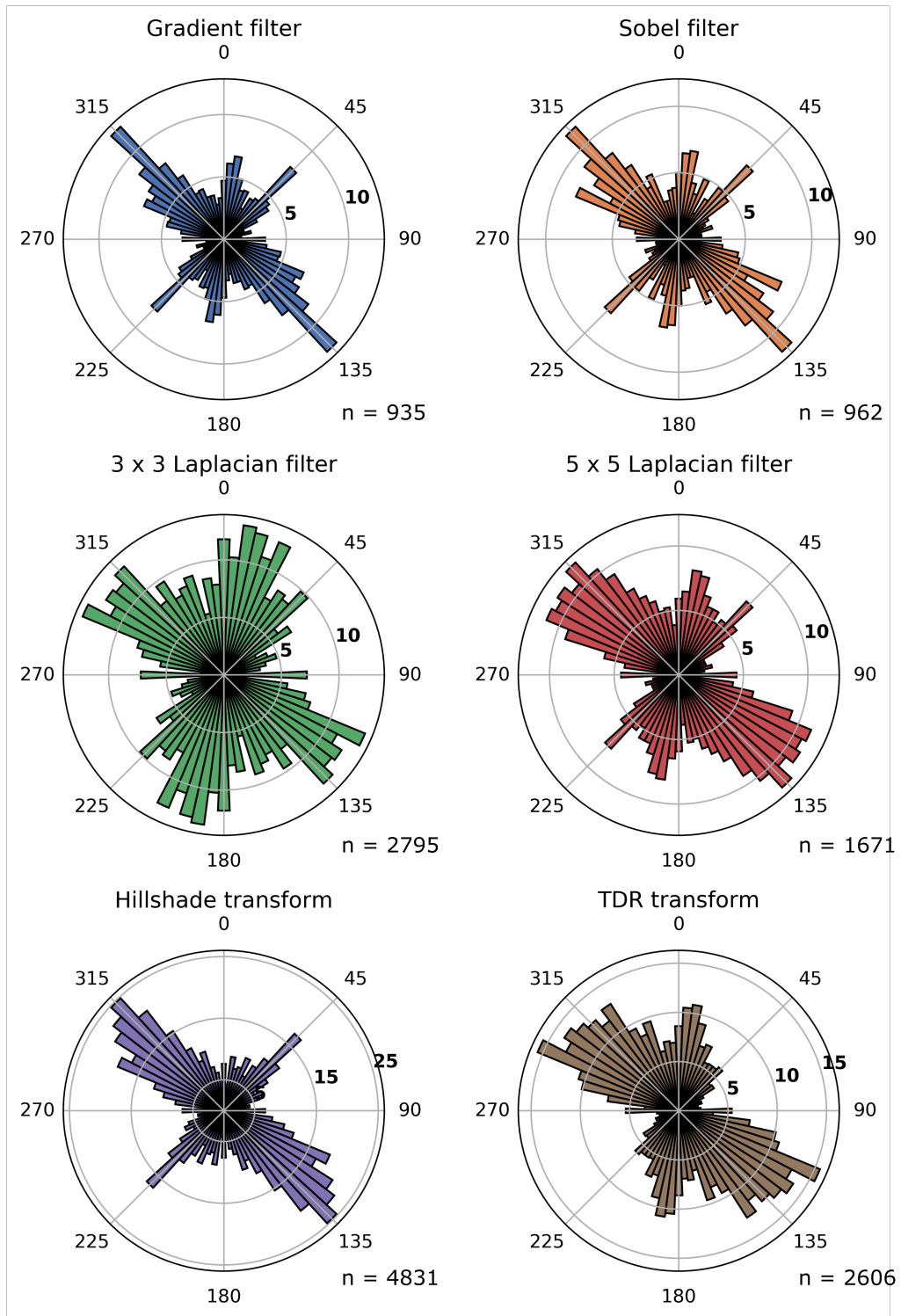


Figure 5: Equal-area wedge rose diagrams for lineament populations derived from each feature extraction technique. The major NW-SE trend is apparent in all plots but with variable clarity. Plots are based on guidelines by Sanderson and Peacock (2020).

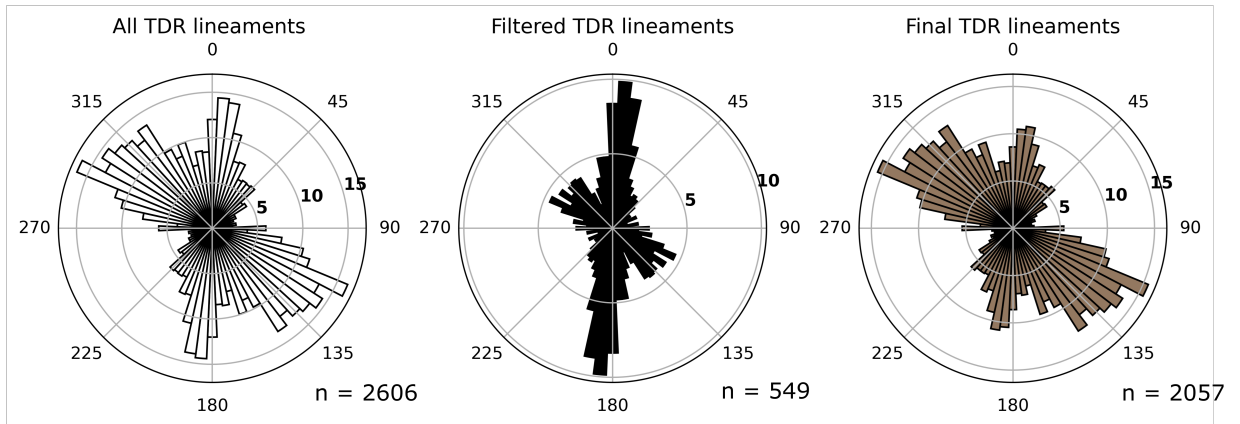


Figure 6: Three rose diagrams where A) is the original population of lineaments for the TDR transform; B) is the population of spurious lineaments; C) the final lineament population for the TDR transform following spatial filtering.

590 **List of Tables**

591 1 Statistical summary of length and depth for each lineament population derived by the six different
592 feature extraction operators (Oper.) where GRAD = gradient filter; LP3 = 3 x 3 Laplacian; LP5 = 5 x
593 5 Laplacian; HS = Hillshade and TDR = tilt derivative. Removed lineaments include those by spatial
594 filtering and parentheses denote those removed due to NaN values. μ = Mean, σ = standard deviation,
595 *Skew* = Skewness and *Kurt* = kurtosis 32

Table 1

Statistical summary of length and depth for each lineament population derived by the six different feature extraction operators (Oper.) where GRAD = gradient filter; LP3 = 3 × 3 Laplacian; LP5 = 5 × 5 Laplacian; HS = Hillshade and TDR = tilt derivative. Removed lineaments include those by spatial filtering and parentheses denote those removed due to NaN values. μ = Mean, σ = standard deviation, *Skew* = Skewness and *Kurt* = kurtosis

Type	Oper.	N	Removed	μ	σ	Median	Range	<i>Skew</i>	<i>Kurt</i>
length	GRAD	935	8	23.67	9.66	20.80	117.49	4.27	30.70
length	Sobel	962	6	22.84	7.54	20.38	78.37	2.97	16.38
length	LP3	2795	7 (1)	25.14	10.14	22.07	96.06	2.46	9.16
length	LP5	1671	0 (2)	28.28	15.50	23.87	194.03	4.06	27.33
length	HS	4831	0	29.71	17.98	24.39	273.62	4.04	28.36
length	TDR	2606	549 (6)	28.97	17.45	23.67	230.14	4.28	29.73
depth	GRAD	935	8	-20.43	7.02	20.80	39.00	-0.09	0.76
depth	Sobel	962	6	-20.66	7.56	20.38	38.95	-0.04	0.20
depth	LP3	2795	7 (1)	-20.16	7.54	22.07	40.49	0.10	0.34
depth	LP5	1671	0 (2)	-19.35	5.51	23.87	38.40	0.25	0.87
depth	HS	4831	0	-20.02	6.81	24.39	39.65	0.06	0.60
depth	TDR	2606	549 (6)	-23.37	8.32	23.67	39.46	0.09	-0.26